Effects of geometric uncertainty on the inverse EEG problem

David M. Weinstein and Christopher R. Johnson

Department of Computer Science
University of Utah
Salt Lake City, UT 84112
{dweinste,crj}@cs.utah.edu

ABSTRACT

A standard method for noninvasively computing neurocortical potentials from potentials measured on the scalp surface is to solve the problem on a generalized geometry and map the results back to the true model. This solution to the inverse EEG problem has been employed using spherical and, more recently, generic cranial models as templates. In the case of the most complex spherical models, the patient's skin, bone, cerebrospinal fluid, gray matter and white matter surfaces are mapped onto concentric spheres. The simplicity of the spherical domain allows for an analytic solution to the surface mapping inverse problem; however, the inaccuracy of such a solution challenges its clinical value. Similarly, solving the problem on a predefined generic model also holds computational allure - the generic model can be hand-picked to reduce the ill-conditioning of the problem. However, we suggest that such results from generic models are still not sufficiently accurate to be of general clinical use. In our paper, we evaluate the impact of varying both model accuracy and model complexity on the inverse cortical mapping. Small modeling perturbations (as might be introduced from noisy or under-sampled data) are shown to have large and detrimental effects on the quality of the solution.

Keywords: inverse EEG problem, finite element method, geometric uncertainty, computational modeling

1. INTRODUCTION

Neurocortical mapping is a fundamental problem in neuroscience. It is at the foundation of surgical planning and prognosis for neurological conditions ranging from epilepsy to schizophrenia,[1] from multiple sclerosis[2] to brain tumors. The goal of cortical mapping is to integrate patient anatomic information and measured voltage potentials from the surface of the patient's scalp in order to **non-invasively** determine what electrical activity is taking place on the patient's cortical surface.[3] In its distilled form, this challenge addresses the basic question: *Which specific regions of the brain are most active at a given moment?* Neuroscience researchers predict that with an answer to this question, their understanding of, and ability to treat, the above mentioned pathologies would stand to profit.

Currently, this question cannot be consistently answered. As a result, clinicians have been analyzing patients using grossly simplified models. These models are incapable of capturing the details of the system, but because they are simple to solve and they generally produce usable approximations to the "true" solution, they are used in patient diagnosis on a daily basis. We propose that a better approach would be to use more geometrically accurate models, but with bounded complexity so as to make them computationally tractable. These models would only incorporate the cranial structures that have the greatest impact on solution accuracy. Unfortunately, it is not currently known which structures contribute most significantly (nor how much each structure contributes to the overall solution/error in a quantitative way) to the accuracy of an inverse-derived cortical mapping.

In this paper, we start to shed light on this question. By running a suite of simulations, we have started to assess the relative impact of geometric complexity and geometric accuracy on inverse EEG mapping.

2. BACKGROUND

2. Theory

Mathematically, the general inverse EEG problem can be posed as an inverse source problem in terms of the primary current sources within the brain, governed by Poisson's equation for electrical conduction:

$$\nabla \cdot \sigma \nabla \Phi = -I_v \quad \text{in } \Omega \tag{1}$$

with the boundary condition:

$$\sigma \nabla \Phi \cdot \mathbf{n} = 0 \quad \text{on } \Gamma_C \tag{2}$$

where Φ are the electrostatic potentials, σ is the conductivity tensor, I_v are the cortical current sources per unit volume, and Γ_C and Ω represent the surface and volume of the cranium, respectively. Unlike the inverse problem of electrical impedance tomography, where the goal is to recover the magnitude and location of the various tissue conductivities, here the conductivities are assumed to be known. The goal is to recover magnitude and location of the neurological sources. In general, (1) does not have a unique solution. In order to solve the general source problem, one usually breaks up the volume of the brain into subregions, within which simplifying assumptions are made regarding the form of the source term (such as dipoles or other equivalent sources). One then tries to recover magnitude and directional information of the simplified model sources. Alternatively, if instead of solving (1) in terms of the current sources within the brain, one solves for the electrostatic potentials on a surface bounding the brain, e.g., the cerebral cortex, this form of the problem does have a unique solution. Thus instead of solving Poisson's equation we solve a generalized Laplace's equation with Cauchy boundary conditions:

$$\nabla \cdot \sigma \nabla \Phi = 0 \tag{3}$$

with boundary conditions:

$$\Phi = \Phi_0 \quad \text{on } \Sigma \subseteq \Gamma_C \quad \text{and} \quad \sigma \nabla \Phi \cdot \mathbf{n} = 0 \quad \text{on } \Gamma_C \tag{4}$$

While this version of the inverse problem has a unique solution,[4] the problem is still mathematically ill-posed in the Hadamard sense; i.e., the solution does not depend continuously on the data, such that small errors in the measurement of the voltages on the scalp can yield unbounded errors in the solution of cortical voltages.

2.1 Simplified models

Initial research in cortical surface mapping was extremely limited in terms of computational resources. As a result, researchers utilized very simple geometric models which could be solved analytically. Such models included the "infinite brain" model and the concentric spheres model. The "infinite brain" model works by assuming that the head is infinite, homogeneous, and isotropic. This technique produced very approximate results, and was never used in clinical practice. A subsequent, more accurate model used concentric spheres to bound the model domain and to integrate inhomogeneities. This allowed for an inhomogeneous model consisting of three to four regions corresponding to skin, skull, and brain (sometimes split into white matter and grey matter).[5] The concentric sphere technique worked by mapping the patient's true anatomic geometry to a spherical model, solving the source mapping problem analytically on the spherical model, and then applying an inverse mapping back to the true anatomy. The results obtained with this method were considerably better than those derived from the "infinite brain" model, and as a result this technique has even been incorporated into a very popular software package, called BESA, which is used clinically around the world every day. However, the accuracy of the results obtained with this model are still far from reliable; it is not uncommon for this software to locate neuro-electric sources *outside of the patient's head.*

2.2 Finite element model

As computational resources have become ever faster and more accessible, there has been a shift to exploring source localization techniques using a discrete, numeric model.[6] One such method for solving the boundary volume problem in (1) or (3) involves approximating the partial differential equations within a finite dimensional subspace and reformulating it in terms of a linear system. For this study we have utilized the finite element method (FEM) to approximate the field equation (1). To accomplish this, we began with the Galerkin formulation of (1); note that this includes the Dirichlet and Neumann boundary conditions,

$$(\sigma \nabla \Phi, \nabla \overline{\Phi}) = -(I_v, \overline{\Phi}) \tag{5}$$

where $\overline{\Phi}$ is an arbitrary test function, which can be thought of physically as a virtual potential field, and the notation, $(\phi_1, \phi_2) \equiv \int_\Omega \phi_1 \phi_2 \, d\Omega$, denotes the inner product in $L_2(\Omega)$. We now use the finite element method to turn the continuous problem into a discrete formulation. First we discretize the solution domain, $\Omega = \bigcup_{c=1}^{N} \Omega_c$, and define a finite dimensional subspace, $V_h \subset V = \{\overline{\Phi} : \overline{\Phi}$ is continuous on $\Omega, \nabla\overline{\Phi}$ is piecewise continuous on $\Omega\}$. We define parameters of the function $\overline{\Phi} \in V_h$ at node points, $\alpha_i = \overline{\Phi}(x_i), i = 1, 2, \ldots, N$ and define the basis functions, $\Psi_i \in V_h$ as linear piecewise continuous functions that take the value 1 at node points and 0 elsewhere. We can then represent the function, $\overline{\Phi} \in V_h$ as:

$$\overline{\Phi} = \sum_{i=1}^{N} \alpha_i \Psi(x_i) \tag{6}$$

such that $\overline{\Phi} \in V_h$ can be written in a unique way as a linear combination of the basis functions, $\Psi_i \in V_h$. The finite element approximation of the original boundary value problem, (1) can be stated as:

$$\text{Find } \Phi_h \in V_h \text{ such that } (\sigma\nabla\Phi_h, \nabla\overline{\Phi}) = -(I_v, \overline{\Phi}) \tag{7}$$

Furthermore, since $\Phi_h \in V_h$ satisfies (7), then we have $(\sigma\nabla\Phi_h, \nabla\Psi) = -(I_v, \Psi_i)$. Finally, since Φ_h itself can be expressed as the linear combination:

$$\Phi_h = \sum_{i=1}^{N} \xi_i \Psi_i(x) \quad \xi_i = \Phi_h(x_i) \tag{8}$$

we can then write (7) as:

$$\sum_{i=1}^{N} \xi_i (\sigma_{ij} \nabla\Psi_i, \nabla\Psi_j) = -(I_v, \Psi_j) \quad j = 1, \ldots, N \tag{9}$$

The finite element approximation of (1) can equivalently be expressed as a system of N equations with N unknowns, $\xi_1, \ldots, \xi_N$ (the electrostatic potentials). In matrix form, the above system is expressed as, $A\xi = b$, where $A = (a_{ij})$ is the global stiffness matrix and has elements $(a_{ij} = (\sigma_{ij}\nabla\Psi_i, \nabla\Psi_j))$, while $b_i = -(I_v, \Psi_i)$ is the vector of source contributions.

The matrix A contains all the geometry and conductivity information and is symmetric and positive definite. Because the basis function differs from zero for only a few intervals, A is very sparse. These features of A significantly affect the strategy for solving the system of equations and will be exploited later in the section on computations.

2.3 Practical considerations

Unfortunately, these finite element (FE) methods have problems as well. While the analytic models suffered from over-simplicity, the FE models tend to have many degrees of freedom, requiring large-scale computational systems to solve them. In the analytic models, fundamental assumptions regarding model topology were inherently flawed, and so it was inconceivable that those techniques would ever accurately capture the physics of current propagation through a complex medium. In contrast, the FE approach is flexible enough that if we accurately model every primitive element in the model, it is possible that we could accurately map scalp potential to cortical potentials. However, if we attempt to accurately model *every* cranial structure in fine enough detail to guarantee a small threshold of error in our solution, the problem very quickly becomes intractable – numerical systems involving tens of millions of elements (and therefore matrices involving millions of variables) arise, bringing even the most powerful supercomputers to their knees. And so it turns out that there is a fundamental trade-off in modeling cortical voltages and currents: inaccurate models are easy to solve, but yield inaccurate results, while overly resolved models result in computationally unmanageable systems.

The solution to this trade-off is generally one of compromise: choose a subset of the details to incorporate in the simulation, discretize this model at the finest level possible which can still be managed computationally, and run the simulation. Research in adaptive FE methods has led to techniques for iteratively refining and de-refining regions of the domain in order to obtain a global consistency in solution accuracy.[7] But the question concerning which anatomic structures to differentiate in the model remains unresolved.

Different materials have different properties of electrical conductivity. As such, if an anatomic structure is composed of a different material than the region surrounding it, then for the full model to be as accurate as possible that

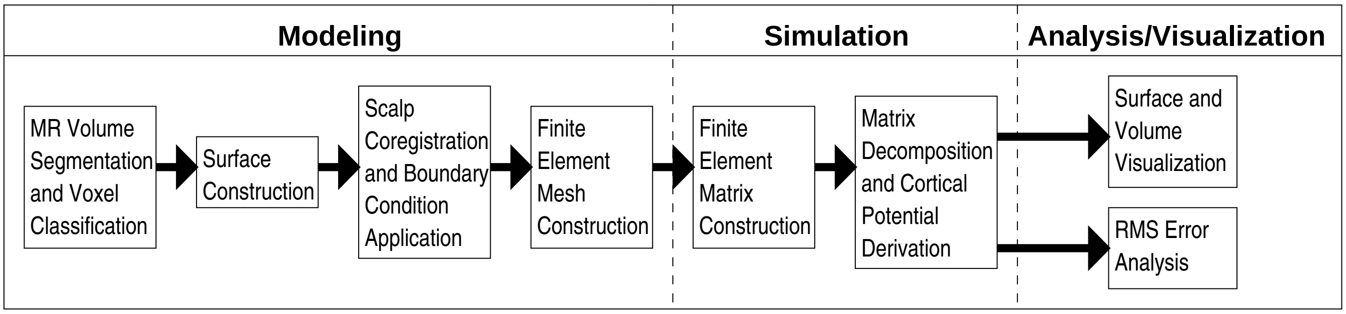

Figure 1: Inverse EEG pipeline for mapping scalp potentials to cortical potentials.

structure must be discretized and modeled with its appropriate conductivity. However, there are two major problems with defining every separate anatomic region in a model. The first is a tractability issue. As we model lots of very small anatomic structures, we are increasing the computational complexity of our model. If these regions aren't critical to how current flows through the system, then we may be wasting computational resources. The second is a human interaction problem. It turns out that many of the anatomic structures in the cranium cannot be identified with automatic computer segmentation algorithms. Instead, an expert must manually label many if not most of the model structures to be incorporated.[8] This manual identification process is very time consuming, often requiring hours of expert interaction to fully label a single structure; furthermore, it is the only non-automated step in the inverse mapping process. It is preferable to minimize the amount of manual segmenting to be performed – only identifying those regions that will have a large impact on the accuracy of the solution. However, at this time, no one has quantitative estimates on how much of an impact any given anatomic structure has on the solution accuracy. In this study, we begin to answer this question.

While the cranial anatomy has never been evaluated in this way before, these methods have been successfully applied to the thoracic regions in electrocardiology (ECG) studies. In 1997, Klepfer, Johnson and MacLeod[9] examined the impact of various thoracic organs on the forward ECG problem. For the study presented here, we extend this earlier work to the cranial domain, now assessing the impact of geometric complexity and accuracy on the inverse EEG problem.

3. IMPLEMENTATION – THE INVERSE EEG PIPELINE

Figure 1 schematically illustrates the "Inverse EEG Pipeline" we have constructed for efficient and interactive surface to surface mapping. Most boxed tasks have been implemented as one of more modules in a SCIRun[10] network. SCIRun is a locally-developed computational steering environment, designed for the modeling, simulation and visualization of large-scale scientific computing applications.

For an even broader scope, the tasks themselves have been visually grouped in the figure into the logical components of modeling, simulation and analysis/visualization. Each task is discussed in detail below.

3.1 MR volume segmentation and voxel classification

Our pipeline takes raw MRI data from a scan of a patient's cranium as anatomic input. This stage of the pipeline is the only stage that has not yet been implemented in SCIRun – rather the segmentation and classification of the volume is accomplished with a statistically-based tool called the EM Segmenter[11] through a collaboration with Harvard Medical School. The output from this process is a tagged volume of voxels, each labeled with a tag to identify the primary material contained within that voxel. For our application, we are specifically interested in: air, skin, bone, cerebrospinal fluid, grey matter and white matter.

3.2 Surface construction

From the classified voxels we extract the set of boundary surfaces via a flood-fill/seed-growing style algorithm. Each boundary then corresponds to a discrete material region. Unfortunately, because the segmentation process can leave some noise in the data, we often have on the order of 10,000 surfaces after this process is completed, with many of these surfaces bounding only a single voxel. To reduce the number of surfaces, we preprocess the segmented volume with a conglomeration algorithm that annexes regions containing less than some threshold number of voxels into the largest neighboring region. This process has the positive effect of reducing the complexity of the model (where fewer surfaces implies lower complexity), but it can also be destructive if the threshold is set too high. As a result, this was one of the parameters we evaluated in this study. The surfaces which result from this extraction have a characteristic "staircase" appearance, since they are composed of voxel faces. To smooth out this data into more physiologically correct (and numerically stable) surfaces, we apply a surface fairing algorithm[12] to these non-manifold surfaces.

3.3 Scalp coregistration and boundary condition application

In addition to the raw MRI data, we use two other clinically obtained raw datasets in our pipeline. These datasets are the basis for the functional data that will be mapped onto the scalp surface, serving as Dirichlet boundary conditions. The first of these datasets are the potentials recorded through electrodes attached to the patient's scalp during a battery of psychological tests. The second dataset is a list of point locations in space, obtained with a pointing device and a magnetic tracker. These points are used to spatially locate the electrode positions on the MR dataset, and consist of electrode positions and a cloud of points digitized from the patient's scalp. The first step in the Coregistration process is to match the point cloud to the scalp surface extracted in the **Surface construction** stage. This is done with a semi-automatic algorithm that applies affine transformations to the point cloud to minimize the summed squared distances from the points in the point cloud to the surface. The second step of this process is to apply the boundary conditions to the scalp surface. We simply determine the closest scalp point to each of the electrodes and assign it the corresponding potential with a Dirichlet boundary condition.

3.4 Finite element mesh construction

To construct our finite element mesh, we use a spatial subdivision algorithm which subdivides space into uniform cubic voxels and places a single mesh node in each voxel. Voxels which correspond to air are not included in this process. The placement of each node is chosen based on two criteria: if a surface passes through the voxel, the node is constrained to lie on the surface; nodes must maintain a minimal distance from each other (a Poisson disk constraint, applied between neighboring voxels is used to guarantee this property). The edge lengths of these cubic voxels will directly determine the number of nodes generated. Since fewer nodes will result in less accurate meshes geometrically, we varied this parameter to evaluate the effect of geometric inaccuracies on the cortical solution. After generating all of the nodes, we insert them one at a time with a Watson-style insertion algorithm[13] to construct a tetrahedral mesh. Each element in the mesh is tagged with a material/conductivity, and any elements located within the cerebral cortex are removed.

3.5 Finite element matrix construction

The finite element matrix is constructed according to the equation (7), and is described in detail in [14]. The result of applying the finite element approximation is a sparse, symmetric, positive-definite stiffness matrix that encodes all of the geometry and conductivity information of the problem.

3.6 Matrix decomposition and cortical potential derivation

To solve for the cortical potentials, given the scalp potentials and the stiffness matrix constructed above, we employ a matrix decomposition described in detail in [15]. In summary, we begin by expressing $A\xi = b$ for the Cauchy problem in (3) as

$$\begin{pmatrix} A_{SS} & A_{SV} & A_{SC} \\ A_{VS} & A_{VV} & A_{VC} \\ A_{CS} & A_{CV} & A_{CC} \end{pmatrix} \begin{pmatrix} \xi_S \\ \xi_V \\ \xi_C \end{pmatrix} = \begin{pmatrix} 0 \\ 0 \\ 0 \end{pmatrix}. \tag{10}$$

We can then rearrange the matrix to solve directly for the cortical voltages in terms of the measured scalp voltages,

$$\xi_C = (A_{SV}A_{VV}^{-1}A_{VC} - A_{SC})^{-1}(A_{SS} - A_{SV}A_{VV}^{-1}A_{VS})\xi_S, \tag{11}$$

where the subscripts, S, V, and C stand for the nodes in the regions of the scalp, volume, and cortex, respectively. In general, the A_{SC} sub-matrix is zero (except for very simple models in which nodes connect directly from the scalp to the cortex). We can then rewrite (11) as

$$\xi_C = (A_{VC}^{-1}A_{VV}A_{SV}^{-1})(A_{SS} - A_{SV}A_{VV}^{-1}A_{VS})\xi_S \tag{12}$$

Note that we now have inverses of three sub-matrices, A_{VC}, A_{SV}, and A_{VV} as well as several other matrix operations to perform. If one estimates the condition number, κ, of the three sub-matrices using the ratio of the maximum to minimum singular values from a singular value decomposition (SVD), one finds that the condition number varies significantly (from $\kappa \approx 200$ for A_{VV} to $\kappa \approx 10^{17}$ for A_{VC} in the most accurate model described below). Thus, one can regularize each of the sub-matrices differently, while leaving some of the sub-matrices untouched from filtering. The overall effect of this *local regularization* is more control over the regularization process.

3.7 Surface and volume visualization

Having solved for the potentials at the cortical nodes in our mesh, one method of evaluating the quality of the results is to verify them visually. We map potentials to colors, and evaluate the potential distribution on the cortical surface. For reference, we also include a volume-rendering[16] of the original MR data coregistered with the scalp and cortical surfaces in the visualization window.

3.8 RMS error analysis

A more quantitative evaluation of the error between two solutions is the standard root-mean-squared difference of the potentials. The RMS error results from our simulations are presented in Table 1, below.

4. RESULTS AND FUTURE DIRECTION

	Number of Nodes			
Number of Voxels	7000	5000	3000	1000
10	0.00%	29.47%	105.03%	661.33%
15	26.48%	30.44%	132.18%	803.27%
20	27.42%	33.45%	209.30%	1297.03%
100	26.26%	40.87%	245.84%	1260.87%

Table 1: RMS error percentages for various levels of model complexity and accuracy.

Table 1 shows the RMS error for each model relative to the solution obtained from the most accurate and complex model. Horizontally, we are decreasing the number of nodes in our model from left to right, while vertically we are ignoring structures beneath of an increasingly large volume threshold progressing from top to bottom. The 10, 15, 20 and 100 voxel minimum volume thresholds yielded models with 107, 77, 58 and 20 independent model regions, respectively. All simulations were run on an SGI Power Onyx with a 90 MHz, R10000 processor with 2 Gb of main memory. The *Matrix decomposition and cortical potential derivation* stage required by far the most significant CPU time for each simulation, and varied from several minutes for the smaller meshes, up to an hour for the most refined meshes.

Figure 2 shows the cortical surface potential maps which resulted from the simulations in the top and bottom rows of Table 1. The most accurate solution is pictured at the top left. We note that while the numeric RMS errors steadily increased across these simulations, the visual degradation is somewhat more abrupt between the images. As the model loses complexity (in terms of the number of disjoint conductivity regions), the solution appears to have only degraded marginally; while as we decrease the number of nodes in the simulation (and thus the degrees of freedom), the visual results rapidly lose fidelity.

To date, there has been very little quantitative understanding of level of accuracy and geometric complexity in modeling cranial current propagation. In this study, we have begun to quantify the effects of these parameters. It is clear from our initial results that modeling accuracy is paramount to solution accuracy. In our next study we plan to evaluate the effects of accuracy in various regions on the domain. It is hypothesized that increased accuracy near regions of high gradients will have the most impact on solution accuracy, while lower resolutions may be substituted in regions of lower gradients without solution degradation. We will run a series of simulations to assess the validity of this hypothesis.

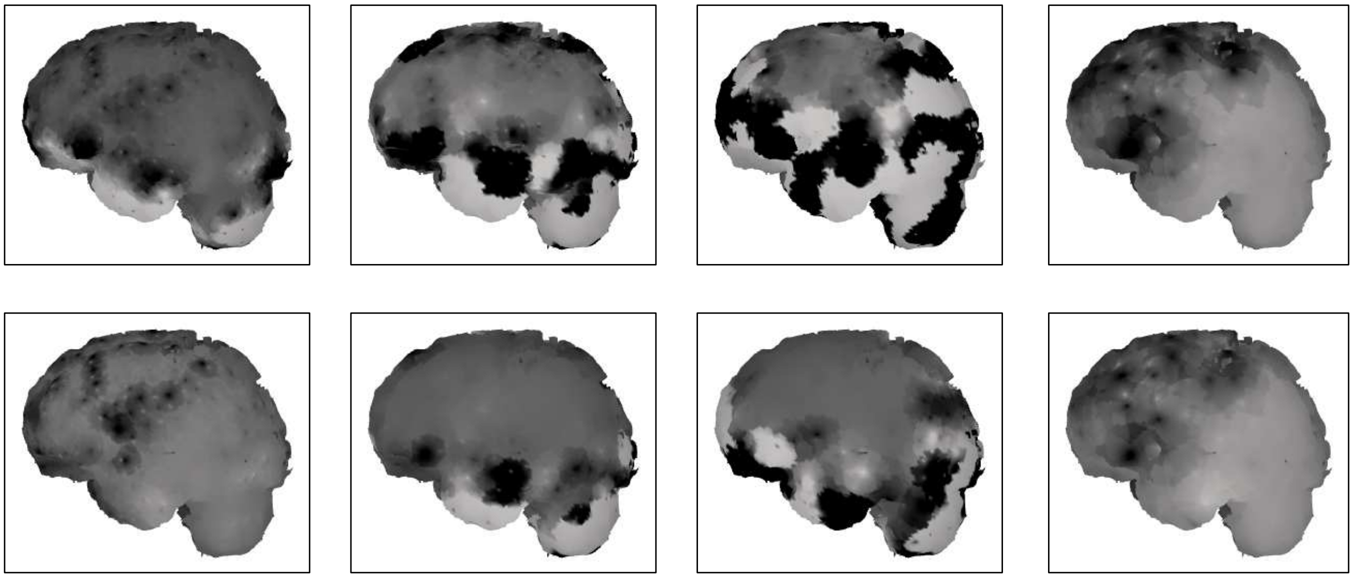

Figure 2: Intensity scaled surface potential maps of the cortex for eight simulations. From left to right the simulations contained 7000, 5000, 3000 and 1000 nodes, respectively. The simulations on the top row contained 107 disjoint conductivity regions, while those on the bottom row contained only 20 disjoint regions.

ACKNOWLEDGMENTS

The authors would like to thank Michelle Miller and Steve Parker for their valuable comments and suggestions. This research was supported in part by awards from the National Science Foundation and the National Institutes of Health. The authors would like to thank Harvard University Medical School for the medical data used in this study.

References

[1] S.F. Faux, R.W. McCarley, P.G. Nestor, M.E. Shenton, S.D. Pollak, V. Penhume, E. Mondrow, B. Marcy, A. Peterson, T. Horvath, and K.L. Davis. P300 topographic assymetries are present in unmedicated schizophrenics. *Electroencephalography and clinical Neurophysiology*, 88:32–41, 1993.

[2] Y. Tada and T. Nagashima. Modeling and simulation of brain lesions by the finite-element method. *IEEE Engineering in Medicine and Biology*, August/September:497–503, 1994.

[3] B. Lutkenhoner, E. Menninghaus, O. Steinstrater, C. Wienbruch, M. Gissler, and T. Elbert. Neuromagnetic source analysis using magnetic resonance images for the construction of source and volume conductor model. *Brain Topography*, 7(4):291–299, 1995.

[4] Y. Yamashita. Theoretical studies on the inverse problem in electrocardiography and the uniqueness of the solution. *IEEE Trans Biomed Eng*, BME-29:719–725, 1982.

[5] S. Homma, T. Musha, Y. Nakajima, Y. Okamoto, S. Blom, R. Flink, K.E. Hagbarth, and U. Mostrom. Location of electric current sources in the human brain estimated by the dipole tracing method of the scalp-skull-brain (ssb) head model. *Electroencephalography and clinical Neurophysiology*, 91:374–382, 1994.

[6] A. Gevins, J. Le, P. Brickett, B. Reutter, and J. Desmond. Seeing through the skull: Advanced eegs use mris to accurately measure cortical activity from the scalp. *Brain Topography*, 4(2):125–131, 1991.

[7] F. Yu and C.R. Johnson. An automatic adaptive refinement and derefinement method. In *Proceedings of the 14th IMACS World Congress*, 1994.

[8] H.W. Shen and C.R. Johnson. Semi-automatic image segmentation: A bimodel thresholding approach. Technical report, UUCS-94-019, Dept. of Computer Science, Univ. of Utah, 1994.

[9] R.N. Klepfer, C.R. Johnson, and MacLeod R.S. The effects of inhomogeneities on electrocardiographic fields: A three-dimensional finite element study. *IEEE Transactions on Biomedical Engineering*, 44(08), 1997.

[10] S.G. Parker, D.M. Weinstein, and C.R. Johnson. The SCIRun computational steering software system. In E. Arge, A.M. Bruaset, and H.P. Langtangen, editors, *Modern Software Tools in Scientific Computing*. Birkhauser Press, 1997 (to appear).

[11] W.M. Wells, W.E.L. Grimson, Kikinis R., and Jolesz F.A. Statistical intensity correction and segmentation of mri data. In *Visualization in Biomedical Computing*, pages 13–24, 1994.

[12] G. Taubin. A signal processing approach to fair surface design. In *ACM SIGGRAPH Computer Graphics*, pages 351–358. IEEE Press, 1995.

[13] D.F. Watson. Computing the n-dimensional dealunay tesselation with applications to voronoi polytopes. *Computer Journal*, 24(2):167–172, 1981.

[14] C. Johnson. *Numerical solution of Partial Differential Equations by the Finite Element Method*. Cambridge University Press, Cambridge, 1990.

[15] D.M. Weinstein, C.R. Johnson, and J.A. Schmidt. Effects of adaptive refinement on the inverse eeg solution. In *Experimental and Numerical Methods for solving Ill-Posed Inverse Problems*, volume 2570. SPIE, 1995.

[16] M. Levoy. Display of surfaces from volume data. *IEEE Comp Graph & Applic*, 8(3):29–37, 1988.